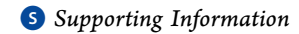
THE JOURNAL OF PHYSICAL CHEMISTRY

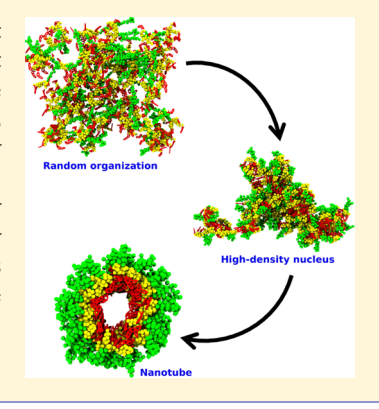
Rational Coarse-Grained Molecular Dynamics Simulations of Supramolecular Anticancer Nanotubes

Anjela Manandhar,^{†,‡} Kaushik Chakraborty,[‡] Phu K. Tang,^{†,‡} Myungshim Kang,[‡] Pengcheng Zhang,[§] Honggang Cui, Honggang Cui, Loverde*,^{†,‡}

¹Department of Oncology and Sidney Kimmel Comprehensive Cancer Center, Johns Hopkins University School of Medicine, Baltimore, Maryland 21205, United States



ABSTRACT: Peptide self-assembly has been used to design an array of nanostructures that possess functional biomedical applications. Experimental studies have reported nanofilament and nanotube formation from peptide-based drug amphiphiles (DAs). These DAs have shown to possess an inherently high drug loading with a tunable release mechanism. Herein, we report rational coarse-grained molecular dynamics simulations of the self-assembly process and the structure and stability of preassembled nanotubes at longer timescales (μ s). We find that aggregation between these DAs at the submicrosecond timescale is driven by directional aromatic interactions between the drugs. The drugs form a large and high-density nucleus that is stable throughout microsecond timescales. Simulations of nanotubes characterize the drug-drug stacking and find correlations at nanometer length scales. These simulations can inform the rational molecular design of drug amphiphiles.



■ INTRODUCTION

Tunable and directional intermolecular forces govern the selfassembly of supramolecular biomaterials. These rationally designed materials have diverse applications in the fields of drug delivery, tissue engineering, and regenerative medicine. Particular to the field of drug delivery, the supramolecular design of classic host-guest complexes has re-emerged with the drug as an active participant.2 The FDA-approved drug Abraxane was the first medicine that employed nanotechnology for the effective delivery of the anticancer drug paclitaxel. Here, paclitaxel was loaded into a protein nanoparticle, which reduced the toxicity and increased the effectiveness of the drug against metastatic breast cancer.^{3,4} Nanostructures have been designed to answer drug delivery challenges such as bioavailability, stability, retention, cytotoxicity, and targeted delivery of the drugs. Generally, to construct these biofunctional nanostructures, a "bottom-up" or "molecular self-assembly" approach is used. This bioinspired method is a free-energy-driven process where an ordered structure is constructed step-by-step starting from disordered building blocks. The greatest advantage of this approach is that the final assembled structure can be fine-tuned by the molecular chemistry of the building blocks, the assembly environment, and the assembly kinetics.⁵

Natural and synthetic peptides have multiple biological purposes as hormones, 9,10 enzyme substrates, 11 ion channel inhibitors, 12,13 antibiotics, 14,15 biological regulators, 16,17 and homing devices for targeted drug delivery. $^{18-20}$ Because of their inherent biocompatibility and biodegradability, peptides are widely used as building blocks of biofunctional nanostructures. With advancements in research and technology, it has become easier to synthesize and characterize a variety of peptide sequences and tune their self-assembly. 21-23 In engineered peptide-containing molecules, the peptide sequence can have a structural or else a bioactive role. Peptides can play a structural role if the components, amino acids, participate in intermolecular interactions driving self-assembly and stabilizing the overall structure, whereas peptides can also play a bioactive role if they are used to recognize biological markers or receptors. Zhang.²⁴ was among the first few groups to show the selfassembly of a short 16-residue peptide into nanofibers. Peptides have been shown to self-assemble into diverse well-organized nanostructures, such as hydrogels, ^{25,26} nanotubes, ^{27–29} bilayers, ^{30,31} nanowires, ³² fibrils, ³³ and so on. Peptides of various

Received: August 3, 2019 Revised: November 18, 2019 Published: November 21, 2019

Department of Chemistry, College of Staten Island, City University of New York, New York 10314, United States

[‡]Ph.D. Program in Biochemistry, The Graduate Center of the City University of New York, New York 10016, United States

Senter of Pharmaceutics, Shanghai Institute of Materia Medica, Chinese Academy of Sciences, Shanghai 201203, China

 $^{^{\}parallel}$ Department of Chemical and Biomolecular Engineering and Institute for NanoBioTechnology, The Johns Hopkins University, Baltimore, Maryland 21218, United States

lengths and types such as linear peptides, $^{34-36}$ cyclic peptides, $^{37-39}$ α -helical, 40,41 β -sheet peptides, $^{42-44}$ and amphiphilic peptides, $^{45-47}$ are used as building blocks for constructing nanostructures.

Peptide amphiphiles (PAs) are a new class of peptide molecules composed of a peptide sequence with a distinct hydrophobic head and hydrophilic tail. 36,48,49 Tirrell et al. 49 designed a PA that self-assembled into collagen-like triplehelical structures. Hartgerink et al.³⁶ designed a PA that assembled to form cylindrical nanofibers. PA nanofibers exhibit interesting photophysical properties, such as the recent study by Fry et al.⁵⁰ that investigated the transport of excitons along chromophores in a self-assembled PA nanofiber. PAs selfassemble into a wide array of nanostructures including vesicles, bilayers, nanofibers, and nanoribbons. 46,51-53 Cylindrical nanofibers formed from these PAs have gained recognition for their biomedical applications such as nerve regeneration⁵⁴ and wound healing, ⁵⁵ as well as their ability to serve as drug delivery vehicles. ^{56–58} Specially, nanotubes assembled from PAs have appeared as one of the most interesting nanostructures for biomedical purposes. These nanotubes have been used to stabilize membrane proteins, ^{59,60} facilitate cell differentiation, ⁶¹ act as drug carriers, ^{28,62} and serve as chemical sensors through functionalization of their surface. These nanotubes possess a high potential for targeted drug delivery with drugs inside the nanotube and functionalized surface with ligands or an antigen targeting specific receptor or an antibody. The driving forces in the self-assembly of these PAs are the noncovalent interactions such as hydrophobic interactions, hydrogen bonding, and electrostatic interactions. 5,66,67 Moreover, external stimuli such as pH, light, temperature, and small molecules have all been shown to modulate the intermolecular interactions altering the structural and mechanical properties of the assembled structures.68-7

Various experimental methods such as light absorption (CD, UV/vis, and IR), wide- or small-angle X-ray scattering (WAXS/ SAXS), and small-angle neutron scattering (SANS) are used to obtain the structural properties of the nanostructure and quantify the intermolecular interactions governing the selfassembly mechanism. 13 However, these experimental methods have their own limitations. The time span of self-assembly can range from nanoseconds to weeks. Experimental methods can succeed in obtaining the structural properties of the final stable structures and some intermediate structures. However, it is still an experimental challenge to understand the initial self-assembly process. Measured quantities such as IR absorption and CD spectra are compared with larger assemblies stabilized by proteins, which might not be valid for smaller systems composed by peptides. Also, these methods provide the average static properties of the system, as opposed to time-dependent properties along the self-assembly pathway. Molecular simulations have emerged as an established method to overcome these experimental limitations. Using computational methods, the dynamic process of self-assembly can be investigated at the molecular level. In the past decade, classical molecular dynamics (MD) simulations have added valuable insights into the understanding of the peptide self-assembly processes. For example, MD simulation has succeeded in characterizing the self-assembly of simple dipeptides such as Phe-Phe into organized nanotubes⁷⁴ and nanowires,⁷⁵ as well as the effect of pH on the self-assembly process of π -conjugated optoelectronic peptides.⁷⁶ MD simulation has the potential to screen the selfassembly properties of peptide mixtures. For example, recently,

MD simulation has been used to characterize nanomorphologies formed by the coassembly of different dipeptides with a tripetide (Asp-Phe-Phe). Furthermore, multiple research groups have utilized both all-atom (AA) and coarse-grained (CG'ed) MD simulations to explore the initial self-assembly process and the stability of resulting PA nanofibers. $^{45,46,78-80}$

Conventionally, nanocarriers have been designed such that drugs are delivered via passive diffusion. In this method, drugs do not participate in the self-assembly mechanism. Drugs are encapsulated in the nanocarrier and stabilized either by noncovalent interactions or through chemical conjugation with the nanocarrier. 81 Recently, Cui et al. 28,62 have designed peptide-based drug amphiphiles (DAs) where the drugs are selfdelivered. Here, the drugs are an important structural component of the building block and participate in the selfassembly mechanism. This approach has been suggested to achieve greater control in drug concentration and distribution in the designed nanocarrier. 81 The DAs used in this study consisted of a short peptide sequence (CGVQIVYKK) and hydrophobic anticancer drug camptothecin, CPT, conjugated via a biodegradable disulfide linker (buss). The peptide sequence consists of the hexapeptide motif (VQIVYKK) known to form β sheet structures leading to tau polymerization and amyloid formation in neurodegenerative diseases.⁸² CPT, a DNA topoisomerase I inhibitor, stabilizes DNA disturbing DNA replication and leads to cell apoptosis. 83 CPT is a challenging drug to formulate due to its low solubility and rapid conversion to a less active carboxylate state under physiological conditions.⁸⁴ Thus, it has been previously suggested to encapsulate CPTs to protect its active lactone state and then transport it to the targeted region.⁸⁵ During self-assembly of these DA molecules, the hydrophobic CPT drugs form the inner core, whereas the peptide forms the outer corona of cylindrical nanostructures. The study reported that increasing the number of conjugated CPTs from one to four resulted in a wider and shorter nanotube (width of 6.70 \pm 1 nm and length of a few micrometers) instead of nanofilament (width of 9.50 \pm 1 nm and length of $<1\mu m$). In another study by Cui et al., 86 using paclitaxel instead of CPT resulted in the formation of nanofilaments (not nanotubes). The critical aggregation concentration of the DA with paclitaxel was almost 50-fold greater compared to that of the DA with CPT, making it less efficient as a model drug delivery system. 87 Herein, we focus on DAs that contain CPTs, which are uniquely found to be stable as

Previous AA and CG'ed MD simulations by Kang et al. 27,88,89 have provided insight into the self-assembly mechanism of these DAs. The simulation studies reported that $\pi - \pi$ stacking between aromatic rings of CPT drugs governs the early stages of the self-assembly process of these cylindrical nanostructures. Indeed, these strongly directional aromatic interactions of the drugs may be driving the initial crystallization of these drugs from the solution. 90 Conventional intermolecular hydrogen bonding between peptide segments was found to be a secondary force that forms in the later stages of the self-assembly process and contributes to the stability of the final morphology. In this study, we perform large-scale CG'ed MD simulations of DAs with four CPTs conjugated to the peptide sequence, which selfassembles into nanotubes.²⁸ This work reports on the CG parametrization of these DAs with four CPTs and long-time (μ s) simulations of the self-assembly of these DAs. Given the long time for assembly into nanotubes (approximately days), we also compare the structure of two preassembled nanotubes that are stable for μ s timescales. We compare our μ s simulations of both the structure and self-assembly of these nanotubes with previous short timescale AA simulations of the exact same systems. Our results support the generality of the CG'ed approach used herein and provide major insights into the selfassembly of these DAs.

We use the Shinoda—Devane—Klein (SDK)^{91–93} approach to CG our DAs and characterize the self-assembly process of these DAs at 1 μ s timescales. In addition, we characterize the stability and structure of preassembled nanotubes. Our CG'ed nanotube successfully reproduces AA self-assembly results.²⁷ We observe the formation of a nonspherical nucleus of DAs from the early stages (<100 ns) of the self-assembly process. This high-density nucleus of DAs, driven by the aggregation of the drugs, is stable throughout the nearly 1.1 µs simulation. Next, we determine the density profile of the nanotube components (CPTs and peptide) in the preassembled nanotubes and find a stable nanotube structure with the hydrophobic CPTs lining the inner radius of the tube and peptides forming the outer surface of the nanotube. These results suggest that these DAs are very likely to self-assemble and can organize into stable nanotubes if the directional aromatic interactions are sufficiently strong. The stability of these nanotubes with CPTs lining the inner radius of these tubes further establishes these nanotubes as a selfdelivering nanocarrier. Furthermore, we demonstrate that the rational CG methods described herein have the potential to capture the initial nucleation mechanisms common to the selfassembly of many pharmaceutical compounds.

METHODS

Coarse-Grained Model of Peptide Drug Amphiphile.

In this study, we perform large-scale CG'ed MD simulations of drug amphiphiles (DAs) with four anticancer drugs CPTs conjugated to the tau peptide sequence (CGVQIVYKK), which self-assemble into nanotubes. We have used the Shinoda-Devane-Klein (SDK)⁹¹⁻⁹³ approach to CG our DAs and have simulated preassembled nanotubes and the self-assembly of these DAs for long timescales ($\sim 1 \mu s$). The SDK approach has been applied to MD simulations of surfactants, 91,94 phospholipid monolayers and bilayers, 93 proteins, 92 polymers, 95,96 and drugs. 88,96 For the SDK CG'ed model of the DA, one CG bead represents two to four heavy atoms and their associated hydrogens, as shown in Figure S1. For the peptides, parameters are directly taken from SDK protein parameters. 92 The parameters for CPT drugs are taken from Kang et al.⁸⁸ where the self-assembly process of these DAs with only one CPT conjugated to the peptide segment was reported.

Here, we develop CG'ed force field parameters for the beads linking CPTs and the peptide using the SDK approach. We use the SDK CG'ed water model,⁹⁷ where three molecules of water is represented by one CG'ed bead. The total potential energy (U) of the CG'ed system is defined as

$$U = U_{\text{bond}} + U_{\text{angle}} + U_{\text{dihe}} + U_{\text{LJ}} + U_{\text{elec}}$$
 (1)

The bonded interactions for bond $(U_{
m bond})$, angle $(U_{
m angle})$, and dihedral (U_{dihe}) are given by harmonic potentials as

$$U_{\text{bond}}(b) = \sum k_{\text{b}}(b - b_{0})^{2}$$
 (2)

$$U_{\text{angle}}(\theta) = \sum k_{\theta}(\theta - \theta_0)^2$$
 (3)

$$U_{\text{dihe}}(\phi) = \sum k_{\phi} [1 + \cos(n\phi - \delta)] \tag{4}$$

where k_b , k_θ , and k_ϕ are the force constants for bond, angle, and dihedral, respectively; b, θ , and ϕ are the bond length, angle, and dihedral angle, respectively, with the subscript zero representing the equilibrium values for the individual terms. n is the periodicity of the torsion and δ is the phase offset.

The nonbonded interactions include Lennard Jones (LJ) and Coulomb potential. LJ (12-4) potential is used for the interaction of DA CG'ed beads, whereas LJ (9-6) potential is used for the interaction of water CG'ed beads and water CG'ed beads with DA CG beads as

$$U_{\text{LJ},12-4}(r) = \sum \frac{3\sqrt{3}}{2} \varepsilon \left(\frac{\sigma^{12}}{r^{12}} - \frac{\sigma^4}{r^4} \right)$$
 (5)

$$U_{\text{LJ},9-6}(r) = \sum \frac{27}{4} \varepsilon \left(\frac{\sigma^9}{r^9} - \frac{\sigma^6}{r^6} \right) \tag{6}$$

where σ is the distance at the LJ minimum, ε is the LJ well depth, and r is the distance between CG'ed sites. In this model, the LJ parameters between pairs of nonidentical CG'ed sites are generated using combination rules in which $\varepsilon_{ii} = \sqrt{\varepsilon_i \varepsilon_i}$ and $\sigma_{ii} =$ $(\sigma_i \sigma_i)/2$. The cutoff is set to 15 Å. While our model is missing direct parametrization of the strength of the $\pi-\pi$ stacking interaction, however, to compensate for this lack of direct parameterization, we effectively increased the LJ parameters of the drug-drug interactions, which are nondirectional. For our CG'ed model, we modify the LJ parameter for the interaction between CPT CG'ed beads such that $\varepsilon_{\text{new}} = 2\varepsilon_{\text{old}}$. Initial simulations with old parameters resulted in distorted nanotube structures; thus, we tested with modified values of $\varepsilon_{\rm new}$ as $2\varepsilon_{\rm old}$ and $4\varepsilon_{\rm old}.$ While $2\varepsilon_{\rm old}$ values stabilized the nanotubes, $4\varepsilon_{\rm old}$ values failed. Our LJ parameters for the CG CPT are mapped from SDK parameters previously reported for surfactants 91,94 and for proteins; 92 however, the parameters are not for aromatic compounds. These LJ parameters were originally obtained by matching the bulk surface tension and density for short-chain surfactants and peptide side-chain analogues. These results suggest a hybrid Boltzmann inversion, 98 and the thermodynamic matching approach could be further refined in the future to better capture strongly directional aromatic interactions. The charged CG'ed beads interact via a Coulomb potential as

$$U(r)_{\text{elec}} = \sum \frac{Cq_i q_j}{\epsilon_i r} \tag{7}$$

where C is an energy conversion constant, q_i and q_j are the charges on the beads *i* and *j* separated by distance *r*, and \in_1 is the effective dielectric constant.

Similar to the parametrization approach by Kang et al., 88 we parametrize the bond, angle, and dihedral potentials using Boltzmann inversion.⁹⁸ The potential of mean force of any internal coordinate q and the probability distribution of q, P(q), is as follows

$$V_{(q)} = -KT \ln(P_{(q)}) \tag{8}$$

After mapping the AA system to a CG'ed model, the interaction site is defined as the center of mass of the selected atoms. Using the previous AA simulations with general amber force field (GAFF),²⁷ bonded interactions for CG interaction sites are parametrized by fitting eqs 2-4 using the last 5 ns of the AA trajectories of the preassembled nanotube. The charge of 0.1118 is assigned to the site of the side chain (L7B and L8B) of lysines (Table S1).92 Each system is neutralized with chloride

ions with a charge of -0.1118 such that the effective dielectric permittivity is uniform throughout the system with \in = 80. The long-range electrostatic interactions are calculated using the particle—particle particle—mesh (PPPM) method. All of the atom parameters, bond parameters, angle parameters, dihedral parameters, and modified LJ parameters are defined in the Supporting Information (Table S2–S5).

Molecular Dynamics Simulations. Two types of CG'ed simulations are explored in this study: (1) randomly organized DAs in a water box (20.1 mM) to study the self-assembly process and (2) preassembled nanotubes (A and B) with different starting orientations of the CPTs in the DA. The starting configuration of the CG'ed random system is mapped from the initial system setup of the all-atom random system, as reported by Kang et al.²⁷ Similarly, the starting configurations for the preassembled nanotubes are mapped from the final structures of the AA simulations (~400 ns) of the same nanotubes by Kang et al.²⁷ For nanotubes A and B, the orientations of the CPTs are in two different starting configurations in the DA. As shown in Figure S2, in the DA of nanotube A, all CPTs are parallel to each other, whereas in the DA of nanotube B, two CPTs are parallel to each other but not all four.

Simulation size and timescales are summarized in Table 1. Each nanotube is infinite due to periodic boundary conditions.

Table 1. System Size, Temperature, and Equilibrated Box Dimensions of Various Systems

system	temperature (K)	total no. of atoms	simulation time (μs)	equilibrated box size $(\mathring{A} \times \mathring{A} \times \mathring{A})$
nanotube A	300	25,461	1	$144 \times 120 \times 112$
nanotube B		29,984	1	$140\times137\times115$
random		109,312	1.1	$146 \times 318 \times 201$

These simulations are performed using the LAMMPS. ¹⁰¹ To increase the efficiency of simulations, each CG'ed drug is treated as a rigid body and the intramolecular interactions are turned off

within rigid CPTs. Simulations are carried out at an anisotropic pressure of 1 atm using the Nose–Hoover thermostat $^{102-104}$ and barostat. 105,106 A two-leveled rRESPA 107 was used such that the bond, angle, and dihedral potentials are evaluated with an inner time step of 2 fs, and the nonbonded interactions are evaluated with the outer time step of 10 fs.

RESULTS

Here, we perform long-time MD simulations ($\sim 1 \mu s$) of CG'ed DAs to characterize the initial aggregation of the DAs into a high-density nucleus of DAs. Movie S1 shows the DAs aggregating to form a high-density nucleus. Figure 1 shows the aggregation and nucleus formation for CG'ed and AA DA simulations. Results for the AA simulation of these DAs are taken from the previous work by Kang et al.²⁷ The initial random organization of DAs is set up using Packmol 108 with a concentration of ~20 mM in a water box (Figure 1A,D). The CG'ed system is simulated for approximately thrice the simulation time compared to the AA system. In both systems, the DAs aggregate to form nuclei of different sizes (Figure 1B,E). Similar to the AA system, we observe planar stacking between neighboring CPTs in the CG'ed system (Figure 1C,F). Next, we investigate the shape and size of these clusters of drugs formed for our CG'ed system. Here, we define a drug cluster based on the distance between CPTs of neighboring DAs. When any CPT of a DA is within 4 Å of CPT of another DA, both DAs are counted as one drug cluster. Figure 2A shows the number of clusters and size of the biggest clusters. We find that the number of drug clusters decreases extremely quickly (within the first 100 ns), suggesting that initial stages of the self-assembly between DAs is driven by the π - π stacking between the CPT drugs. The number of DA clusters decreases to \sim 3 by the end of simulation. The formation of a very large cluster, a nucleus containing nearly all DA molecules, is observed during the initial 100 ns. The system has 96 DAs in total, and the nucleus consists of more than 80 DAs. This nucleus formed during the initial simulation stage remains stable throughout the approximately 1.1 μ s simulation.

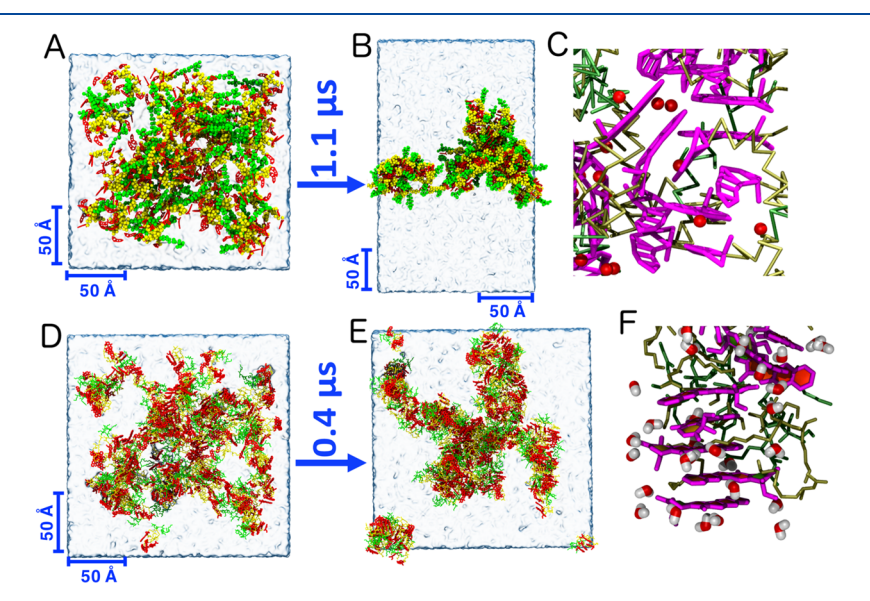


Figure 1. Self-assembly of peptide drug amphiphiles (DAs). Coarse-grained MD simulation. (A) Initial random organization of DAs. (B) Formation of a high-density nucleus of DAs after approximately 1.1 μ s. Here, CPT drugs, linker, and peptide are represented by red, yellow, and green, respectively. (C) Zoomed view showing parallel stacking of CPTs (pink) with each CG water bead (red) within 5 Å of CPTs. Each CG water bead represents three AA water molecules. All-atom MD simulation of same system. (D) Initial random organization of DAs. (E) Aggregate formation after 0.4 μ s. (F) Zoomed view showing parallel stacking of CPTs with water molecules within 5 Å of CPTs.

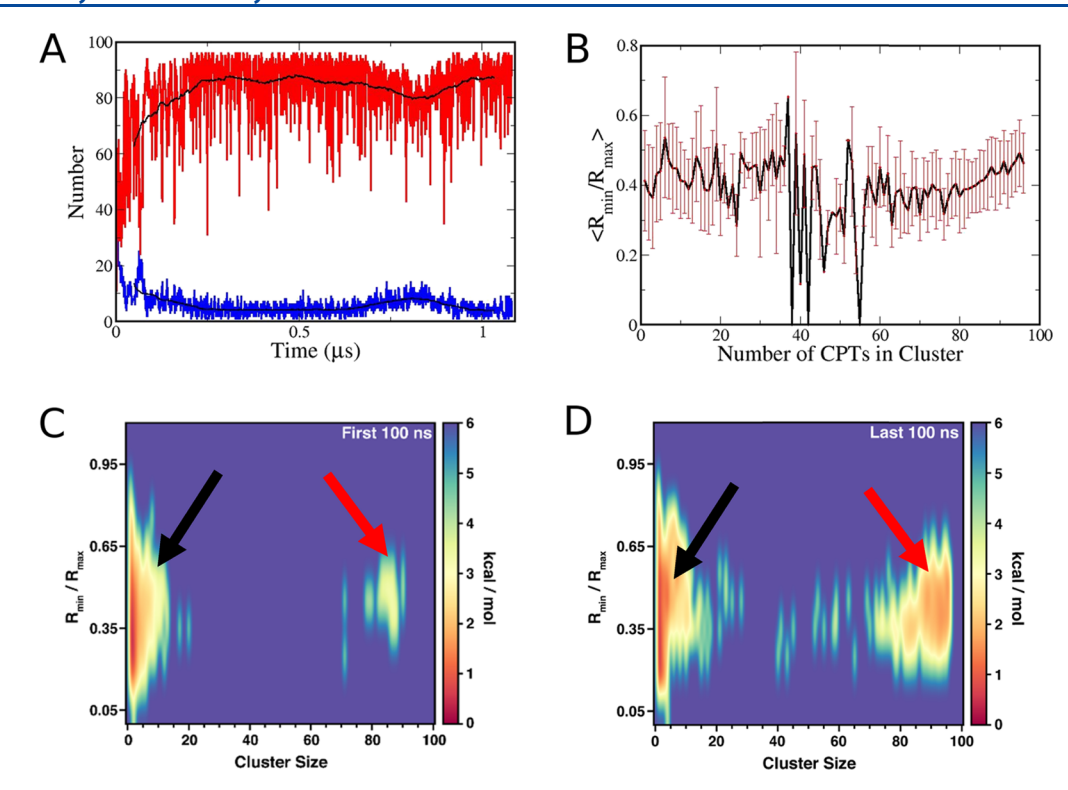


Figure 2. (A) Cluster formation from randomly organized DAs over \sim 1.1 μ s simulation time. We observe the number of clusters (blue) decreases to \sim 3 and the biggest cluster (red) is a combination of \sim 90 DAs. (B) Average R_{\min}/R_{\max} ratio deviates from 1 for all cluster sizes, indicating an elongated, nonspherical cluster growth. 2D-PMF of R_{\min}/R_{\max} ratio as a function of cluster size. (C) First 100 ns and (D) last 100 ns simulations. Along with smaller clusters (black arrow), bigger clusters (red arrow) are formed in early stages of the simulation, which is dominant and stable through the end of the simulation. Both small and big clusters have R_{\min}/R_{\max} ratio deviated from 1, <0.6 indicating that the cluster growth is anisotropic.

Figure 2B shows the shape of the DA clusters. Here, we calculate the ratio of $R_{\rm min}/R_{\rm max}$ where $R_{\rm max}$ is the maximum radius of gyration and $R_{\rm min}$ is the minimum radius of gyration of the specific cluster. Radius of gyration ($R_{\rm G}$) is calculated as

$$R_{\rm G} = \frac{(r_1^2 + r_2^2 + ...r_N^2)}{N} \tag{9}$$

Here, r_1 , r_2 , ... r_N is the distance between the center of mass (COM) of CPT beads and the COM of the cluster (summing over peptide, linker, and CPTs) along the xy plane, and N is the total number of beads. Irrespective of the cluster size, the $R_{\rm min}/R_{\rm max}$ ratio is always less than 1. For the nucleus with more than 80 CPTs from different DAs, the $R_{\rm min}/R_{\rm max}$ ratio is about 0.5. Thus, the nucleus is nonspherical in shape and grows in an anisotropic fashion dominated by the planarity of the aromatic CPT stacking interactions. These observations are further highlighted in the 2D-potential of mean force (PMF) of the $R_{min}/R_{\rm max}$ ratio as a function of cluster sizes (Figure 2C,D). The 2D-PMF is calculated as

$$G(R_{\min/\max}, C_s) = -k_B T[\ln p(R_{\min/\max}, C_s) - \ln p_{\max}]$$
(10)

Here, $R_{\min/\max}$ is the R_{\min}/R_{\max} ratio, C_s is the cluster size, and p_{\max} is the maximum probability.

During the initial 100 ns of the simulation (Figure 2C), small clusters of size less than 10 DAs are most dominant, whereas one much larger nucleus of drugs is just beginning to form. For the last 100 ns simulation (Figure 2D), the population of smaller clusters of size less than 10 DAs still exists, but the largest nucleus of size $\sim 80-90$ DAs is increasingly dominant. These 2DPMFs further support the anisotropic growth of these

clusters. For all cluster sizes, the $R_{\rm min}/R_{\rm max}$ ratio deviates from 1, indicating nonspherical, elongated clusters. Compared to AA simulation of these DAs,²⁷ we find faster cluster formation (in the first 0.4 μ s). As shown in Figure S3, by the end of 0.4 μ s simulation, the AA system has ~10 clusters whereas the CG system has around ~5 clusters. In both systems, we observe a sharp decrease in the number of clusters in the first 100 ns, further supporting the quick self-assembly of these DAs. In our CG'ed model, we doubled the strength of the LJ attractive potential for the CPT beads, as discussed in the Methods section, which might have facilitated this increased attraction between these DAs.

Next, we calculate the static structure factor, S(q), for the CPT drugs and peptide chain. S(q) describes the intensity of light scattered from aggregates of varying sizes and is commonly used for studying the ordering of peptide amphiphiles, copolymers, and polymer membranes. Here, we calculate the static structure factor as a function of scattering vector, q, as

$$S(q) = \frac{1}{N^2} \left\langle \left| \sum_{i,j}^{N} e^{iq\Delta r_{ij}} \right| \right\rangle \tag{11}$$

Here, i and j are the CPT beads, Δr_{ij} is the distance between those beads, N is an integer ranging from 1 to N, and q is the scattering vector defined as

$$q = \frac{2\pi}{\lambda} \tag{12}$$

Here, λ is the size of the aggregates.

As shown in Figure 3, we calculate the S(q) averaged over the first and last 100 ns simulations for both CPT and peptide beads.

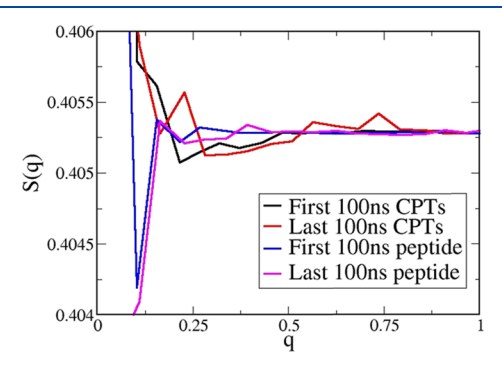


Figure 3. Static structure factor for initial and final 100 ns for CPT beads and peptide beads in random organization of DAs. We observe that CPTs and peptides are more organized at the later stage of simulation compared to initial state.

We observe a higher peak magnitude of S(q) at wavevectors, q^* , for the last 100 ns compared to initial 100 ns for the CPTs. In comparison, the S(q) for the peptide chains for the first and last 100 ns are not significantly different. For the last 100 ns, we find two dominant peaks for the CPTs at $\lambda^* = \frac{2\pi}{q^*}$ values of ~27.3 and ~8.4 Å suggesting CPTs are ordered and periodic at these distances. We also observe ordered peptide chains at λ^* value of ~17.5 Å. The different λ^* values for initial and last 100 ns simulations suggest, during the self-assembly, that the CPTs are rearranging into more ordered domains. Furthermore, the large, stable nucleus throughout the majority of the simulation involves the rearrangement of these multiple, ordered smaller CPT aggregates. As suggested by Mansbach and Ferguson, the self-assembly of peptides containing aromatic groups may follow a Smoluchowski coagulation process. 113

Next, we preassemble two different nanotubes (A and B) with different starting orientations of the CPTs in the DA mapped from the final structures of the AA simulations of the same nanotubes by Kang et al.²⁷ Nanotubes A and B have slightly different starting configurations for the stacking interactions of the CPT drugs, as further discussed in the Methods section. The

relaxed widths of nanotube A and nanotube B are 10.43 ± 0.37 and 9.33 ± 0.32 nm, respectively, which is consistent with the experimentally reported width of the DA nanotubes of 9.5 \pm 1 nm. We note that to maintain the stability of the nanotube, CPT-CPT interactions are strengthened accordingly, as described in more detail in the Methods section. Figure 4 shows the relaxed nanotube A structure after the 1 μ s simulation where CPT, linker, and peptide are shown in red, green, and yellow, respectively. The CPTs line the inner radius of the tube forming a hydrophobic surface in contact with a narrow channel of water while the peptide forms the outer surface of the nanotube. The CGed nanotubes A and B are stable throughout the simulation with hydrophobic drugs forming the inner core and peptides forming the outer corona. We find that the aromatic CPT drugs stack along the dimensions of the nanotube (Figure 4C), as observed in the AA simulation (Figure 4D). We first compare the radial density distribution of each component, CPT, peptide, and water, of the last 100 ns of CG'ed nanotubes with the last 50 ns of the AA nanotubes.²⁷ Figure 4E shows a transmission electron microscopy (TEM) image showing that nanotubes formed from the self-assembly of qCPTs at 50 μ M concentration. Next, we analyze the orientation and stacking of CPTs, followed by analysis of the water diffusion in the narrow center channel of the nanotube compared with the surface of the nanotube.

As seen in Figure 5, we observe that the radial density distributions are fairly conserved between the AA and CG'ed simulations. We find that the radial density distribution range of each component in both nanotubes in CG'ed and AA models is similar: the hydrophobic inner channel of the nanotubes is filled with water with the inner surface of the nanotubes lined by hydrophobic CPTs and the outer surface of nanotube lined by the hydrophilic peptides. Both nanotubes have an inner radius of \sim 15 Å and outer radius of \sim 45 Å. The peak for the radial distribution for each component in the CG'ed model is slightly shifted inward toward the core compared to that in the AA model.

Next, we characterize the radial density distribution of charges, Cl^- ions and protonated amines (NH_3^+) , of the lysines. Figure 6A shows the distribution of these charged elements in nanotube A. We see that Cl^- ions (red) are both inside the hydrophobic inner channel of the nanotube as well as outside

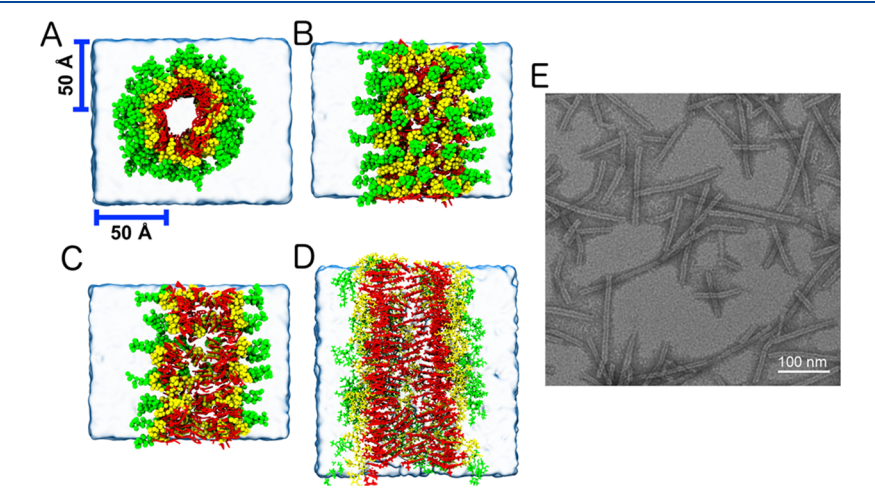


Figure 4. Coarse-grained nanotube after 1 μs simulation where CPT, linker, and peptide are represented in red, yellow, and green, respectively. (A) Top, (B) side, and (C) sliced views. (D) Sliced view of all-atom nanotube showing stacked CPTs similar to the CG model. (E) Transmission electron microscopy image of the nanotubes formed with 50 μM qCPTs.

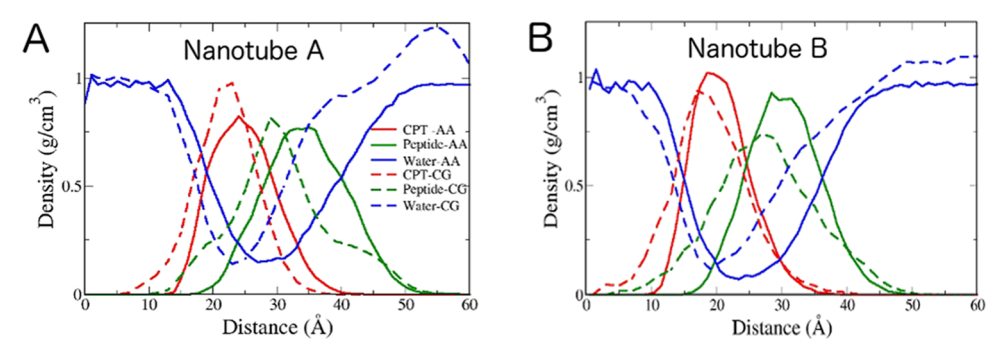


Figure 5. Radial density distribution of CPT (red), peptide (green), and water (blue) in all-atom (solid lines) and coarse-grained (dotted lines) models of (A) nanotube A and (B) nanotube B.

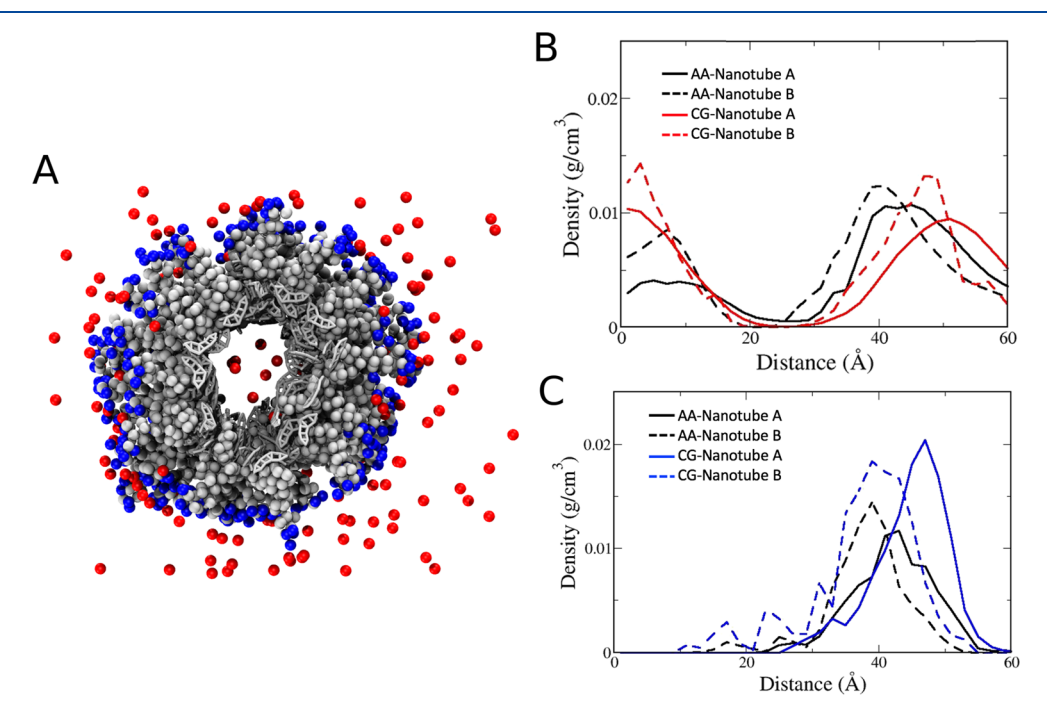


Figure 6. (A) Charge distribution around nanotube A. Here, Cl^- ions and protonated amines (NH_3^+) are colored red and blue, respectively. (B) Cl^- ions are found inside and around the nanotubes. (C) NH_3^+ of lysines are around the outer surface of the nanotubes.

the surface of the nanotube. The protonated amines (blue) are on the nanotube, forming an outer charged hydrophilic surface. Figure 6B,C shows the comparative radial density distribution of Cl⁻ ions and NH₃⁺ of lysines, respectively, for nanotubes A and B. For both nanotubes, we find that the Cl⁻ ions are distributed both inside and outside the nanotube. The peak of Cl⁻ ion distribution is at the center of the hydrophobic channel and also at the outer surface of the nanotubes, showing strong counterion condensation. For the NH₃⁺ of lysines, the charge is distributed on the nanotube's outer surface. The peak value of NH₃⁺ distribution for nanotube A is at ~48 Å, whereas for nanotube B, it is at ~39 Å. The charge distribution characteristic of both nanotubes compares well with the AA results.²⁷ The high density of positively charged lysines around the nanotubes leads to a fairly high surface charge density of ~+.48/nm² and a line charge density of +14.4/nm. Due to the high +ve surface charge density, a large number of Cl⁻ counterions are condensed close to the surface of the tube.

It has been reported that pK_a can shift during protein folding and peptide self-assembly. For example, in a protein-based polymer, polypentapeptides, the pK_a of the aspartic acid side chain carboxylic acid shifts to 6.1 (normal pK_a value = 3.65). 114

Similarly, in *Staphylococcus* nuclease, the p K_a for glutamic acids is reported to shift up to a value of 9.4 (normal p K_a value = 4.2). Another study in *Staphylococcus* nuclease reported that the p K_a of lysines is reduced to a value of 6.2 (normal p K_a value = 10.5). Studies have reported the hydrophobic environment with restricted access to bulk water as one of the major reasons for these observed p K_a shifts. Our nanotubes are "set up" at neutral pH 7 with protonated amine side chains of the lysines. Since these lysine residues are exposed to solvent, we do not expect large p K_a shifts as observed for internal residues of proteins. However, if there is a p K_a shift for our system, then the amines of lysines would be deprotonated and the nanotubes would be a neutral system.

Next, we compare the orientation of CPTs with respect to the radial vector and axis of the nanotube. The radial vector is the axis formed by the COM of the CPT and COM of the nanotube in the xy plane. The CPT axis is the longest axis along the CPT. The CPT orientation in CG'ed nanotubes compares well with that in the AA nanotubes (Figure 7). As seen in Figure 7A (left panel), CPTs in the AA nanotube A possess a preferred tilt in the range of $\sim 20-30^{\circ}$ with respect to the radial vector, whereas the CG nanotube has a preferred tilt with a greater range of $\sim 20-30^{\circ}$

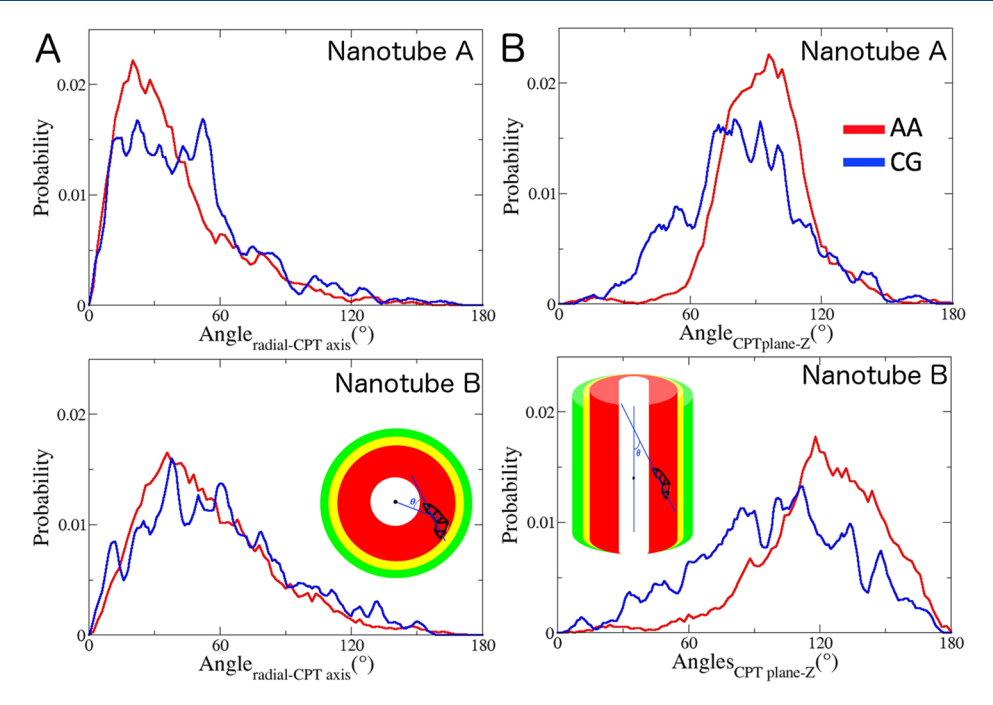


Figure 7. CPT orientation. (A) Distribution of angles between the radial vector and the long CPT axis in nanotubes A and B. (B) Distribution of angles between the axis of the tube and the CPT planes in nanotubes A and B.

50°. For nanotube B, there is a better agreement between AA and CG'ed nanotubes, with a peak tilt angle at ~36°. For the orientation of CPTs with respect to nanotube axis, we observe that CG'ed nanotubes have a wider range of preferred tilts compared to AA nanotubes. As seen in Figure 7B (right panel), AA nanotube A has a peak at \sim 90°, whereas CG nanotube A has a preferred tilt in the range of 70-100°. Similarly, for AA nanotube B, the preferred CPT tilt with respect to nanotube axis is \sim 120°, whereas for CG'ed nanotube B, the most preferred tilt is in the range of 100–115°. The average angles throughout the simulation (Figure S4) show that nanotubes A and B do not converge during the $\sim 1~\mu s$ simulation timescale. At later stages of simulation, we observe that the average angle between the CPT plane and nanotube axis is $\sim 80^{\circ}$ for nanotube A and $\sim 100^{\circ}$ for nanotube B (Figure S4A). Similarly, at later stages of simulation, the average angle between the CPT plane and radial vector is ~45° for nanotube A and ~58° for nanotube B (Figure S4B). This analysis shows that both nanotubes A and B are equilibrated by the end of the $\sim 1 \mu s$ simulation with stable orientations of CPTs with respect to the nanotube axis and radial vector. Next, we compare the total energy of interactions between DA-DA, DA-solvent, and solvent-solvent of nanotubes A and B during the $\sim 1 \mu s$ simulations (Figure S5A). We find that nanotube B has a lower energy compared to nanotube A. We compare the bond, angle, dihedral, van der Waals (VDW), and electrostatic energies (Figure S5B-F). We find the that VDW and angle energies are the main contributing factors for the lower energy of nanotube B compared to nanotube A, indicating the configuration and packing of the CPTs.

To characterize stacking of the planar CPTs in the core of nanotubes (Figure 8A), we calculate the stacking correlation of the angles between CPTs as a function of distance between them along the nanotube axis. The correlation function, $\langle C(r,\theta) \rangle$, is calculated as $C(r,\theta)=1$ when $|\theta| \leq \theta_{\rm cut}$ and $C(r,\theta)=0$ when $|\theta| > \theta_{\rm cut}$ where $\theta_{\rm cut}$ is the cutoff angle of 30°. We observe slightly different correlation profiles (Figure 8B) for nanotubes A and B. We find that both CG'ed nanotubes A and B have one fold

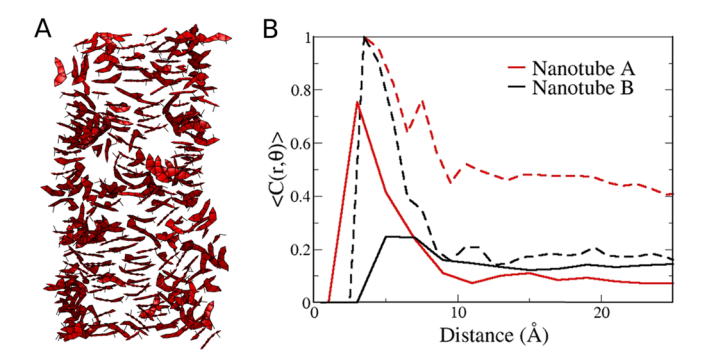


Figure 8. (A) Stacking observed between aromatic rings of CPT drugs along the nanotube axis. (B) Stacking correlation between CPT planes as function of distance along the nanotube axis in all-atom (dashed line) and CG'ed (solid lines) in nanotube A (red) and nanotube B (black).

stacking with peaks at d < 5 Å. The AA nanotubes A and B display a second peak (7 Å < d < 15 Å). The observed stacking correlation for the CG'ed model is only 1-fold compared to that for the AA model with 3-fold stacking. Also, the height of the peaks is reduced in both nanotubes A and B for the CG'ed model compared to the AA model. Thus, in the CG'ed model, planar stacking is reduced compared to the AA model.

Next, we characterize the diffusion of water inside and around the nanotube A using the mean squared displacement with respect to time. This is calculated as 118

$$\langle r^2 \rangle = \langle |r_i(t) - r_i(0)^2| \rangle \tag{13}$$

As shown in Figure 9A, we differentiate the water into three types based on their respective position: (i) in-tube water, which is the water inside the hydrophobic channel of the nanotube from the center to 15 Å in the *xy* plane, (ii) surface water, which is the water around the nanotube from 15 to 45 Å in the *xy* plane, and (iii) bulk water, which is the water outside the nanotube. As shown in Figure 9B, we observe that the surface water has the lowest diffusion and the bulk water has the highest diffusion. The

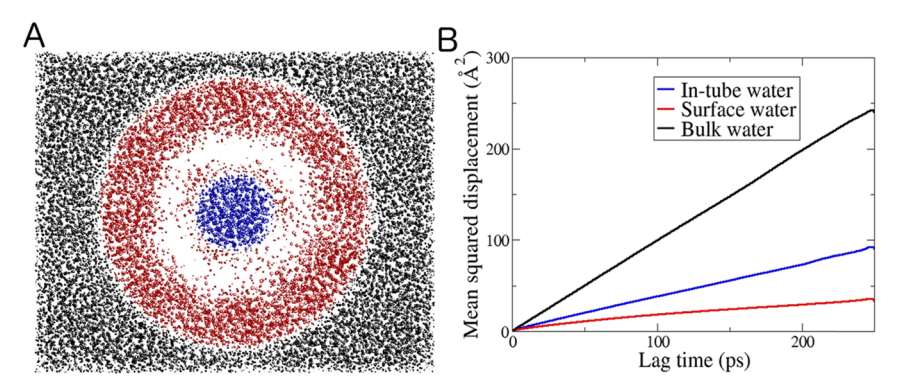


Figure 9. (A) Water differentiated based on proximity with the nanotube: in-tube, surface, and bulk water as shown in blue, red, and black, respectively. (B) Water diffusion of in-tube water is more similar to that of bulk water, and surface water has lower diffusion due to interaction with DAs.

lowest diffusion of surface water is the result of water interactions with the nanotube components; similarly, slower diffusion of in-tube water should be due to the confinement of water in the tube. We also calculate the diffusion coefficients and compare with AA results (Table 2).²⁷ The diffusion coefficient is

Table 2. Water Diffusion Coefficients in All-Atom and Coarse-Grained Nanotube A

water type	coarse-grained (m^2/s)	all-atom (m^2/s)
bulk water	3.30×10^{-9}	3.2×10^{-9}
in-tube water	1.24×10^{-9}	2.2×10^{-9}
surface water	0.52×10^{-9}	0.9×10^{-9}

determined by fitting the diffusion curve to the equation, $r^2 =$ 2nDt, ¹¹⁹ where r is the displacement, n = 3 is the dimension, t is time lag, and D is the diffusion coefficient. We obtain a similar trend of diffusion coefficients for both models. We find that the diffusion coefficient for the bulk water is almost the same for both models, whereas for in-tube water and surface water, it decreases by $\sim 1/2$ in the CG'ed model.

CONCLUSIONS

Herein, we present rational CG'ed MD simulations of the selfassembly process of these DAs at timescales of nearly 1 μ s. We find that the initial stages of the self-assembly process are governed by the strength of the aromatic interactions between the conjugated aromatic drugs. We observe the formation of a large high-density nucleus of DAs within the first 100 ns that is stable throughout the $\sim 1.1 \, \mu s$ simulation. These aggregates are anisotropic and elongate in one direction. Indeed, the formation of this high-density phase containing the DAs is reminiscent of two-step nucleation models for the formation of crystalline solids. ¹²⁰ This suggests that the rational CG methods described herein have the potential to capture the initial nucleation mechanisms common to the self-assembly of many pharmaceutical compounds. The preassembled nanotubes are stable throughout the 1 μ s simulations with CPTs forming the inner lining of the nanotube core and peptides forming the outer surface. We find that the planar stacking between CPTs is reduced in the CG'ed model compared to the AA model, but the trend persists.

Fine-tuning the rational CG'ed models presented within can further characterize the aggregation of the DAs into wellorganized nanotubes at longer timescales. For our approach, we used the Boltzmann inversion method⁹⁸ to determine the bond, angle, and dihedral potentials for our CG'ed model and combine

these with LJ parameters determined from thermodynamic approaches. Here, the π - π interaction is not explicitly included, and lack of this interaction is a limitation for our CG'ed model. An alternative method, namely, force matching (FM), 121,122 has been used to derive CG potentials with forces matching the AA system. This method has been successfully used to generate CG potentials for peptides ^{122,123} and biomolecules. ^{124,125} Next, Shell et al. 126 have used relative entropy minimization (REM) to optimize CG potentials mimicking the target AA system. This approach has been used to study the self-assembly of CG'ed polyalanines. 127 Moreover, adding a directional H-bonding potential might be another alternative. This directional Hbonding potential might facilitate β -sheet formation between peptide chains. As reported by Chen et al., directional Hbonds between DAs can be added as defined by the normal plane of three beads. The formation of β -sheet can align CPTs of different DAs in planar orientation facilitating π – π stacking. Thus, directional H-bonds can be a compensatory potential to facilitate π – π interaction missing in our CG model. Although there is no significant difference in the number of H-bonds during polypeptide self-assembly,³³ addition of a directional Hbonding potential to peptide force fields has the potential to impact future computational studies of short polypeptide self-assembly and their phase behavior. 129,130

Herein, we perform simulations with periodic repeats of short nanotube sections. In future research, finite-sized long nanotubes can be simulated to investigate the length-dependent effects on the structural and mechanical properties of nanotubes. Moreover, future research can examine the effect of external factors such as pH, salt concentration, and temperature on the self-assembly process and nanotube stability. Together, this line of research can provide valuable insights into the optimal conditions for the self-assembly of DAs and PAs and their rational design.

ASSOCIATED CONTENT

S Supporting Information

The Supporting Information is available free of charge at https://pubs.acs.org/doi/10.1021/acs.jpcb.9b07417.

Figures S1-S5, aggregation and growth of DAs comparing AA and CG models, mapping for CG'ed model of the DA, and initial setup of the DA conformation in nanotubes; Tables S1-S5, list of CG parameters; and Table S6, scaling and CPU hours for AA and CG'ed systems (PDF)

Movie S1, aggregation of randomly organized DAs into an ordered high-density nucleus (MP4)

AUTHOR INFORMATION

Corresponding Author

*E-mail: sharon.loverde@csi.cuny.edu. Phone: 718-982-4075.

ORCID ®

Myungshim Kang: 0000-0002-4778-8240 Pengcheng Zhang: 0000-0002-4546-0022 Honggang Cui: 0000-0002-4684-2655 Sharon M. Loverde: 0000-0002-7643-6498

Author Contributions

The manuscript was written through contributions of all authors. All authors have given approval to the final version of the manuscript.

Notes

The authors declare no competing financial interest.

ACKNOWLEDGMENTS

This research was supported, in part, by the NSF through TeraGrid resources under grant number TG-CHE130099 and a grant of computer time from the City University of New York High Performance Computing Center under NSF grant nos. CNS-0855217, CNS-0958379, and ACI-1126113. S.M.L. acknowledges start-up funding received from the College of Staten Island and City University of New York. S.M.L. would also like to acknowledge NSF grant nos. DMR-1506937 and DMR-1255281 and NIH grant no. 1R15EB020343. A.M. would like to acknowledge partial support from the Rosemary O'Halleran scholarship.

ABBREVIATIONS

MD molecular dynamics

AA all-atom

CG coarse-grained

DA drug amphiphile

peptide amphiphile

REFERENCES

- (1) Webber, M. J.; Appel, E. A.; Meijer, E. W.; Langer, R. Supramolecular biomaterials. Nat. Mater. 2016, 13-26.
- (2) Webber, M. J.; Langer, R. Drug delivery by supramolecular design. Chem. Soc. Rev. 2017, 46, 6600-6620.
- (3) Yardley, D. A. nab-Paclitaxel mechanisms of action and delivery. J. Controlled Release 2013, 365-372.
- (4) Nyman, D. W.; Campbell, K. J.; Hersh, E.; Long, K.; Richardson, K.; Trieu, V.; Desai, N.; Hawkins, M. J.; Von Hoff, D. D. J. Clin. Oncol. **2005**, 23, 7785-7793.
- (5) Paramonov, S. E.; Jun, H. W.; Hartgerink, J. D. J. Am. Chem. Soc. 2006, 128, 7291-7298.
- (6) Liu, K.; Xing, R.; Zou, Q.; Ma, G.; Möhwald, H.; Yan, X. Angew. Chem., Int. Ed. 2016, 55, 3036-3039.
- (7) Pashuck, E. T.; Cui, H.; Stupp, S. I. J. Am. Chem. Soc. 2010, 132,
- (8) Manandhar, A.; Kang, M.; Chakraborty, K.; Tang, P. K.; Loverde, S. M. Org. Biomol. Chem. 2017, 15, 7993-8005.
- (9) Kaiser, E. T.; Kezdy, F. J. Amphiphilic secondary structure: design of peptide hormones. Science 1984, 223, 249-255.
- (10) Wilcox, G. Insulin and Insulin Resistance. Clin. Biochem. Rev. 2005, 26, 19-39.
- (11) Troitskaya, L. A.; Kodadek, T. Methods 2004, 32, 406-415.
- (12) Zhang, A. H.; Sharma, G.; Undheim, E. A. B.; Jia, X.; Mobli, M. A complicated complex: Ion channels, voltage sensing, cell membranes and peptide inhibitors. Neurosci. Lett. 2018, 679, 35-47.
- (13) Diochot, S.; Salinas, M.; Baron, A.; Escoubas, P.; Lazdunski, M. Toxicon 2007, 49, 271-284.

- (14) Kleinkauf, H.; von Döhren, H. Crit. Rev. Biotechnol. 2008, 8, 1-32.
- (15) Hancock, R. E. W.; Chapple, D. S. Peptide Antibiotics. Antimicrob. Agents Chemother. 1999, 43, 1317-1323.
- (16) Cunha, F. M.; Berti, D. A.; Ferreira, Z. S.; Klitzke, C. F.; Markus, R. P.; Ferro, E. S. J. Biol. Chem. 2008, 283, 24448-24459.
- (17) Perego, M. PLoS Biol. 2013, 11, No. e1001516.
- (18) Boohaker, R. J.; Lee, M. W.; Vishnubhotla, P.; Perez, J. L. M.; Khaled, A. R. The Use of Therapeutic Peptides to Target and to Kill Cancer Cells. Curr. Med. Chem. 2012, 19, 3794-3804.
- (19) Habibi, N.; Kamaly, N.; Memic, A.; Shafiee, H. Self-assembled peptide-based nanostructures: Smart nanomaterials toward targeted drug delivery. Nano Today 2016, 41-60.
- (20) Fosgerau, K.; Hoffmann, T. Drug Discovery Today 2015, 20, 122-128.
- (21) Wegmuller, S.; Schmid, S. Curr. Org. Chem. 2014, 18, 1005-1019.
- (22) Zhao, X.; Pan, F.; Lu, J. R. Prog. Nat. Sci. 2008, 18, 653-660.
- (23) Tamerler, C.; Sarikaya, M. ACS Nano 2009, 3, 1606-1615.
- (24) Zhang, S. Nat. Biotechnol. 2003, 21, 1171-1178.
- (25) Xing, R.; Li, S.; Zhang, N.; Shen, G.; Möhwald, H.; Yan, X. Biomacromolecules 2017, 18, 3514-3523.
- (26) Schneider, J. P.; Pochan, D. J.; Ozbas, B.; Rajagopal, K.; Pakstis, L.; Kretsinger, J. J. Am. Chem. Soc. 2002, 124, 15030-15037.
- (27) Kang, M.; Chakraborty, K.; Loverde, S. M. J. Chem. Inf. Model. 2018, 58, 1164-1168.
- (28) Cheetham, A. G.; Zhang, P.; Lin, Y. A.; Lock, L. L.; Cui, H. J. Am. Chem. Soc. 2013, 135, 2907-2910.
- (29) Wang, Q.; Zhang, X.; Zheng, J.; Liu, D. Self-assembled peptide nanotubes as potential nanocarriers for drug delivery. RSC Adv. 2014, 4, 25461-25469.
- (30) Li, S.; Mehta, A. K.; Sidorov, A. N.; Orlando, T. M.; Jiang, Z.; Anthony, N. R.; Lynn, D. G. J. Am. Chem. Soc. 2016, 138, 3579-3586.
- (31) Natarajan, P.; Sukthankar, P.; Changstrom, J.; Holland, C. S.; Barry, S.; Hunter, W. B.; Sorensen, C. M.; Tomich, J. M. ACS Omega 2018, 3, 11071-11083.
- (32) Ryu, J.; Park, C. B. Biotechnol. Bioeng. 2010, 105, 221-230.
- (33) Su, Z.; Dias, C. L. J. Phys. Chem. B 2014, 118, 10830-10836.
- (34) Choi, S.-j.; Jeong, W.-j.; Kang, S.-K.; Lee, M.; Kim, E.; Ryu, D. Y.; Lim, Y.-b. Biomacromolecules 2012, 13, 1991-1995.
- (35) Mandal, D.; Shirazi, A. N.; Parang, K. Org. Biomol. Chem. 2014, 12, 3544-3561.
- (36) Hartgerink, J. D.; Beniash, E.; Stupp, S. I. Science 2001, 294, 1684-1688.
- (37) Khurana, E.; Nielsen, S. O.; Ensing, B.; Klein, M. L. J. Phys. Chem. B 2006, 110, 18965-18972.
- (38) Mandal, D.; Tiwari, R. K.; Nasrolahi Shirazi, A.; Oh, D.; Ye, G.; Banerjee, A.; Yadav, A.; Parang, K. Soft Matter 2013, 9, 9465-9475.
- (39) Ghadiri, M. R.; Granja, J. R.; Milligan, R. A.; McRee, D. E.; Khazanovich, N. Nature 1993, 366, 324-327.
- (40) Mondal, S.; Gazit, E. ChemNanoMat. 2016, 323-332.
- (41) Smith, A. M.; Banwell, E. F.; Edwards, W. R.; Pandya, M. J.; Woolfson, D. N. Adv. Funct. Mater. 2006, 16, 1022-1030.
- (42) Tao, H.; Lee, S. C.; Moeller, A.; Roy, R. S.; Siu, F. Y.; Zimmermann, J.; Stevens, R. C.; Potter, C. S.; Carragher, B.; Zhang, Q. Nat. Methods 2013, 10, 759-761.
- (43) Kim, S.; Kim, J. H.; Lee, J. S.; Park, C. B. Small 2015, 11, 3623-3640.
- (44) Bowerman, C. J.; Liyanage, W.; Federation, A. J.; Nilsson, B. L. Biomacromolecules 2011, 12, 2735-2745.
- (45) Velichko, Y. S.; Stupp, S. I.; De La Cruz, M. O. J. Phys. Chem. B 2008, 112, 2326-2334.
- (46) Cui, H.; Webber, M. J.; Stupp, S. I. Self-assembly of peptide amphiphiles: From molecules to nanostructures to biomaterials. Pept. Sci. 2010, 94, 1-18.
- (47) Fleming, S.; Ulijn, R. V. Design of nanostructures based on aromatic peptide amphiphiles. Chem. Soc. Rev. 2014, 43, 8150-8177.
- (48) Aida, T.; Meijer, E. W.; Stupp, S. I. Science 2012, 335, 813-817.

- (49) Gore, T.; Dori, Y.; Talmon, Y.; Tirrell, M.; Bianco-Peled, H. *Langmuir* **2001**, *17*, 5352–5360.
- (50) Solomon, L. A.; Sykes, M. E.; Wu, Y. A.; Schaller, R. D.; Wiederrecht, G. P.; Fry, H. C. ACS Nano 2017, 11, 9112–9118.
- (51) Kokkoli, E.; Mardilovich, A.; Wedekind, A.; Rexeisen, E. L.; Garg, A.; Craig, J. A. Soft Matter 2006, 2, 1015–1024.
- (52) Hartgerink, J. D.; Beniash, E.; Stupp, S. I. *Proc. Natl. Acad. Sci. U. S. A.* **2002**, *99*, 5133–5138.
- (\$3) Dehsorkhi, A.; Castelletto, V.; Hamley, I. W. J. Pept. Sci. **2014**, 20, 453–467.
- (54) Tysseling-mattiace, V. M.; Sahni, V.; Niece, K. L.; Birch, D.; Czeisler, C.; Fehlings, M. G.; Stupp, S. I.; Kessler, J. A. J. Neurosci. 2008, 28. 3814–3823.
- (55) Hosseinkhani, H.; Hong, P.-D.; Yu, D.-S. Self-Assembled Proteins and Peptides for Regenerative Medicine. *Chem. Rev.* **2013**, *113*, 4837–4861.
- (56) Rezler, E. M.; Khan, D. R.; Lauer-Fields, J.; Cudic, M.; Baronas-Lowell, D.; Fields, G. B. *J. Am. Chem. Soc.* **2007**, *129*, 4961–4972.
- (57) Zhang, P.; Cheetham, A. G.; Lin, Y. A.; Cui, H. ACS Nano 2013, 7, 5965-5977.
- (58) Toft, D. J.; Moyer, T. J.; Standley, S. M.; Ruff, Y.; Ugolkov, A.; Stupp, S. I.; Cryns, V. L. ACS Nano **2012**, *6*, 7956–7965.
- (59) Zhao, X.; Nagai, Y.; Reeves, P. J.; Kiley, P.; Khorana, H. G.; Zhang, S. *Proc. Natl. Acad. Sci.* **2006**, *103*, 17707–17712.
- (60) Matsumoto, K.; Vaughn, M.; Bruce, B. D.; Koutsopoulos, S.; Zhang, S. J. Phys. Chem. B **2009**, 113, 75–83.
- (61) Silva, G. A.; Czeisler, C.; Niece, K. L.; Beniash, E.; Harrington, D. A.; Kessler, J. A.; Stupp, S. I. *Science* **2004**, *303*, 1352–1355.
- (62) Lin, Y.-A.; Cheetham, A. G.; Zhang, P.; Ou, Y.-C.; Li, Y.; Liu, G.; Hermida-Merino, D.; Hamley, I. W.; Cui, H. ACS Nano **2014**, 8, 12690—12700.
- (63) Douberly, G. E.; Pan, S.; Walters, D.; Matsui, H. J. Phys. Chem. B **2001**, 105, 7612–7618.
- (64) Banerjee, I. A.; Yu, L.; Matsui, H. J. Am. Chem. Soc. 2003, 125, 9542-9543.
- (65) Matsui, H.; MacCuspie, R. Nano Lett. 2001, 1, 671-675.
- (66) Toksöz, S.; Guler, M. O. Nano Today 2009, 458-469.
- (67) Stendahl, J. C.; Rao, M. S.; Guler, M. O.; Stupp, S. I. Adv. Funct. Mater. 2006, 16, 499–508.
- (68) Mart, R. J.; Osborne, R. D.; Stevens, M. M.; Ulijn, R. V. Soft Matter 2006, 2, 822-835.
- (69) Freeman, R.; Han, M.; Álvarez, Z.; Lewis, J. A.; Wester, J. R.; Stephanopoulos, N.; McClendon, M. T.; Lynsky, C.; Godbe, J. M.; Sangji, H.; Luijten, E.; Stupp, S. I. Science 2018, 362, 808–813.
- (70) Leung, C.-Y.; Palmer, L. C.; Qiao, B. F.; Kewalramani, S.; Sknepnek, R.; Newcomb, C. J.; Greenfield, M. A.; Vernizzi, G.; Stupp, S. I.; Bedzyk, M. J.; Olvera de la Cruz, M. ACS Nano 2012, 6, 10901–10000
- (71) Lin, Y.; Penna, M.; Thomas, M. R.; Wojciechowski, J. P.; Leonardo, V.; Wang, Y.; Pashuck, E. T.; Yarovsky, I.; Stevens, M. M. ACS Nano 2019, 13, 1900–1909.
- (72) Ulijn, R. V.; Smith, A. M. Chem. Soc. Rev. 2008, 37, 664-675.
- (73) Frederix, P. W. J. M.; Patmanidis, I.; Marrink, S. J. *Chem. Soc. Rev.* **2018**, *47*, 3470–3489.
- (74) Jeon, J.; Mills, C. E.; Shell, M. S. J. Phys. Chem. B 2013, 117, 3935–3943.
- (75) Reches, M.; Gazit, E. Science 2003, 300, 625-627.
- (76) Mansbach, R. A.; Ferguson, A. L. Org. Biomol. Chem. 2017, 15, 5484–5502.
- (77) Moreira, I. P.; Scott, G. G.; Ulijn, R. V.; Tuttle, T. Mol. Phys. **2019**, 117, 1151–1163.
- (78) Lee, O.-S.; Stupp, S. I.; Schatz, G. C. J. Am. Chem. Soc. 2011, 133, 3677–3683.
- (79) Yu, T.; Schatz, G. C. J. Phys. Chem. B 2013, 117, 9004-9013.
- (80) Tekin, E. D. Molecular dynamics simulations of self-assembled peptide amphiphile based cylindrical nanofibers. *RSC Adv.* **2015**, *5*, 66582–66590.

- (81) Lu, H.; Wang, J.; Wang, T.; Zhong, J.; Bao, Y.; Hao, H. Recent Progress on Nanostructures for Drug Delivery Applications. *J. Nanomater.* **2016**, 2016, 20.
- (82) Goux, W. J.; Kopplin, L.; Nguyen, A. D.; Leak, K.; Rutkofsky, M.; Shanmuganandam, V. D.; Sharma, D.; Inouye, H.; Kirschner, D. A. *J. Biol. Chem.* **2004**, 279, 26868–26875.
- (83) Pommier, Y. Nat. Rev. Cancer 2006, 6, 789-802.
- (84) Li, F.; Jiang, T.; Li, Q.; Ling, X. Am. J. Cancer Res. 2017, 7, 2350—
- (85) Soukasene, S.; Toft, D. J.; Moyer, T. J.; Lu, H.; Lee, H. K.; Standley, S. M.; Cryns, V. L.; Stupp, S. I. *ACS Nano* **2011**, *5*, 9113–9121
- (86) Lin, R.; Cheetham, A. G.; Zhang, P.; Lin, Y.-a.; Cui, H. Supramolecular filaments containing a fixed 41% paclitaxel loading. *Chem. Commun.* **2013**, *49*, 4968–4970.
- (87) Ma, W.; Cheetham, A. G.; Cui, H. Nano Today 2016, 13-30.
- (88) Kang, M.; Cui, H.; Loverde, S. M. Soft Matter 2017, 13, 7721–7730.
- (89) Kang, M.; Zhang, P.; Cui, H.; Loverde, S. M. Macromolecules **2016**, 49, 994–1001.
- (90) Erdemir, D.; Lee, A. Y.; Myerson, A. S. Polymorph selection: the role of nucleation, crystal growth and molecular modeling. *Curr. Opin. Drug Discovery Dev.* **2007**, *10*, 746–755.
- (91) Shinoda, W.; Devane, R.; Klein, M. L. Multi-property fitting and parameterization of a coarse grained model for aqueous surfactants. *Mol. Simul.* **2007**, *33*, 27–36.
- (92) DeVane, R.; Shinoda, W.; Moore, P. B.; Klein, M. L. J. Chem. Theory Comput. **2009**, *5*, 2115–2124.
- (93) Shinoda, W.; Devane, R.; Klein, M. L. Soft Matter 2008, 4, 2454—2462.
- (94) Shinoda, W.; Discher, D. E.; Klein, M. L.; Loverde, S. M. Soft Matter 2013, 9, 11549–11556.
- (95) Drenscko, M.; Loverde, S. M. Mol. Simul. 2017, 43, 234-241.
- (96) Loverde, S. M.; Klein, M. L.; Discher, D. E. *Adv. Mater.* **2012**, *24*, 3823–3830.
- (97) He, X.; Shinoda, W.; Devane, R.; Klein, M. L. Mol. Phys. 2010, 108, 2007–2020.
- (98) Reith, D.; Pütz, M.; Müller-Plathe, F. J. Comput. Chem. 2003, 24, 1624–1636.
- (99) De Joannis, J.; Arnold, A.; Holm, C. J. Chem. Phys. 2002, 117, 2503–2512.
- (100) Cerdà, J. J.; Ballenegger, V.; Lenz, O.; Holm, C. J. Chem. Phys. **2008**, 129, 234104.
- (101) Plimpton, S. J. Comput. Phys. 1995, 117, 1-19.
- (102) Kamberaj, H.; Low, R. J.; Neal, M. P. J. Chem. Phys. 2005, 122, 224114.
- (103) Hoover, W. G. Phys. Rev. A 1985, 31, 1695-1697.
- (104) Tuckerman, M.; Berne, B. J.; Martyna, G. J. J. Chem. Phys. 1992, 97, 1990–2001.
- (105) Martyna, G. J.; Tobias, D. J.; Klein, M. L. J. Chem. Phys. 1994, 101, 4177-4189.
- (106) Parrinello, M.; Rahman, A. J. Appl. Phys. 1981, 52, 7182-7190.
- (107) Tuckerman, M. E.; Alejandre, J.; López-Rendón, R.; Jochim, A. L.; Martyna, G. J. J. Phys. A: Math. Gen. 2006, 39, 5629–5651.
- (108) Martínez, L.; Andrade, R.; Birgin, E. G.; Martínez, J. M. J. Comput. Chem. 2009, 30, 2157-2164.
- (109) Brunello, G. F.; Mateker, W. R.; Lee, S. G.; Choi, J. I.; Jang, S. S. Effect of temperature on structure and water transport of hydrated sulfonated poly(ether ether ketone): A molecular dynamics simulation approach. *J. Renewable Sustainable Energy* **2011**, *3*, No. 043111.
- (110) Jo, W. H.; Kim, J. G.; Jang, S. S.; Youk, J. H.; Lee, S. C. *Macromolecules* **1999**, 32, 1679–1685.
- (111) Jang, S. S.; Molinero, V.; Çağın, T.; Goddard, W. A. J. Phys. Chem. B **2004**, 108, 3149–3157.
- (112) Jang, S. S.; Goddard, W. A. J. Phys. Chem. C 2007, 111, 2759–2769.
- (113) Mansbach, R. A.; Ferguson, A. L. J. Phys. Chem. B 2017, 121, 1684–1706.

- (114) Urry, D. W.; Gowda, D. C.; Peng, S.; Parker, T. M.; Jing, N.; Harris, R. D. *Biopolymers* **1994**, *34* (7), 889–896.
- (115) Isom, D. G.; Castañeda, C. A.; Cannon, B. R.; Velu, P. D.; García-Moreno, E. B. *Proc. Natl. Acad. Sci. U. S. A.* **2010**, *107* (37), 16096–16100.
- (116) Isom, D. G.; Castañeda, C. A.; Cannon, B. R.; García-Moreno, E. B. *Proc. Natl. Acad. Sci. U. S. A.* **2011**, *108* (13), 5260–5265.
- (117) Wu, X.; Lee, J.; Brooks, B. R. J. Phys. Chem. B 2017, 121 (15), 3318-3330.
- (118) Chakraborty, K.; Bandyopadhyay, S. J. Chem. Phys. 2015, 143, No. 045106.
- (119) Allen, M. P.; Tildesley, D. J. Computer simulation of liquids; Oxford University Press: 1987.
- (120) Erdemir, D.; Lee, A. Y.; Myerson, A. S. Acc. Chem. Res. 2009, 42, 621–629.
- (121) Izvekov, S.; Voth, G. A. J. Phys. Chem. B 2005, 109 (7), 2469–2473
- (122) Zhou, J.; Thorpe, I. F.; Izvekov, S.; Voth, G. A. *Biophys. J.* **2007**, 92 (12), 4289–4303.
- (123) Thorpe, I. F.; Goldenberg, D. P.; Voth, G. A. J. Phys. Chem. B **2011**, 115 (41), 11911–11926.
- (124) Izvekov, S.; Chung, P. W.; Rice, B. M. J. Chem. Phys. **2010**, 133 (6), No. 064109.
- (125) Shi, Q.; Izvekov, S.; Voth, G. A. J. Phys. Chem. B **2006**, 110 (31), 15045–15048.
- (126) Shell, M. S. J. Chem. Phys. 2008, 129 (14), 144108.
- (127) Carmichael, S. P.; Shell, M. S. J. Phys. Chem. B 2012, 116 (29), 8383-8393.
- (128) Imamura, H.; Chen, J. Z. Y. Proteins: Struct., Funct., Genet. 2006, 63 (3), 555–570.
- (129) Chu, W.; Qin, J.; De Pablo, J. J. Macromolecules **2018**, *51* (5), 1986–1991.
- (130) Dignon, G. L.; Zheng, W.; Kim, Y. C.; Best, R. B.; Mittal, J. *PLoS Comput. Biol.* **2018**, *14* (1), No. e1005941.